

Chapter 5

Lower mantle structure from paleogeographically constrained dynamic Earth models

To be submitted as:

Bower, D. J., M. Gurnis, and M. Seton (2012), Lower mantle structure from paleogeographically constrained dynamic Earth models, *Geochem. Geophys. Geosy.*

5.1 Abstract

Seismic tomography reveals two large, low-shear velocity provinces (LLSVPs) beneath Africa and the Pacific Ocean. These structures may have existed for several 100 Myrs and are likely compositionally distinct based on observed seismic, geodynamic, and mineral physics characteristics. We investigate the dynamics of the LLSVPs through the use of evolutionary models of thermochemical structures from 250 Ma to present day. We use a 3-D spherical convection model in which the anomalous structures have a high bulk modulus, consistent with seismic interpretation. A new progressive assimilation method incorporates constraints from paleogeography using a refined plate history model (with 1 Myr time spacing) to guide the thermal structure of

the lithosphere and steer the thermal evolution of slabs in the uppermost mantle. The thermochemical structures deform and migrate along the core-mantle boundary (CMB), either by coupling to plate motions or in response to slab stresses. The models produce a ridge-like anomaly beneath Africa and a rounded pile beneath the Pacific Ocean. However, slabs from the Tethys Ocean push the African structure further to the southwest than inferred from tomography. Dense and viscous slabs can severely compromise the stability of high bulk modulus structures at the CMB.

5.2 Introduction

Seismic tomography (Fig. 5.1a,b) reveals two large, low-shear velocity provinces (LLSVPs) at the base of the mantle beneath Africa and the Pacific Ocean with approximately a degree-two pattern. These structures contain 1.5–2.4 vol. % and ~ 2 mass % of the mantle and occupy almost 20% surface area of the core-mantle boundary (CMB) (e.g., *Hernlund and Houser, 2008; Burke et al., 2008*). A thermochemical origin is necessary to explain anti-correlated shear wave and bulk sound velocity anomalies (*Su and Dziewonski, 1997; Masters et al., 2000*), putative anti-correlated shear wave and density anomalies (*Ishii and Tromp, 1999, 2004*), multipathing for waves sampling its steep edges (*Ni et al., 2002*), and geological inferences of stability over 200–300 Myr (*Burke and Torsvik, 2004*). Waveform modeling identifies the finer-scale structure and refines the geographical extent of the LLSVPs. This technique is particularly useful to address ambiguity in tomography models by resolving the vertical extent of the structures and the wavespeed reduction and thickness of the

basal layer.

Ritsema et al. (1998) present compelling evidence for a large mid-mantle structure beneath Africa by satisfying travel-time data for S, ScS, and SKS, along a corridor from the Drake passage to the Hindu Kush. The African LLSVP rises 1500 km above the CMB with an S wavespeed reduction of 3%. This is also supported by the first arrival cross over of SKS to S from South American events to world-wide standard seismographic network (WWSSN) stations in Africa (*Ni et al.*, 1999). These early studies identify strong shear velocity gradients at the edges and top of the structure. *Ni et al.* (2002) attribute SKS waveform complexity to in-plane (2-D) multipathing and use the travel-time delays to determine a boundary width of less than 50 km. They further suggest the eastern edge of the bulk of the anomaly is tilted toward the northeast, in agreement with some tomography models (*Ritsema et al.*, 1999) (Fig. 5.1c). Alternatively, *Wang and Wen* (2007a) use more data from events northeast of the anomaly to argue that this flank tilts to the center and the basal layer extends farther northeast.

The thickness and velocity reduction of the basal layer at the CMB beneath the African structure remains contentious. Beneath the eastern part of the South Atlantic, *Wen et al.* (2001) propose a 300-km-thick anomaly with much lower S wavespeeds linearly decreasing from -2% at the top to about -10% at the base (also see *Wen*, 2002). P and S core reflected phases support this interpretation (*Simmons and Grand*, 2002). *Wen* (2001) extend this feature beneath the Indian Ocean by modeling several corridors of data and ascribe travel-time delays to variations in layer

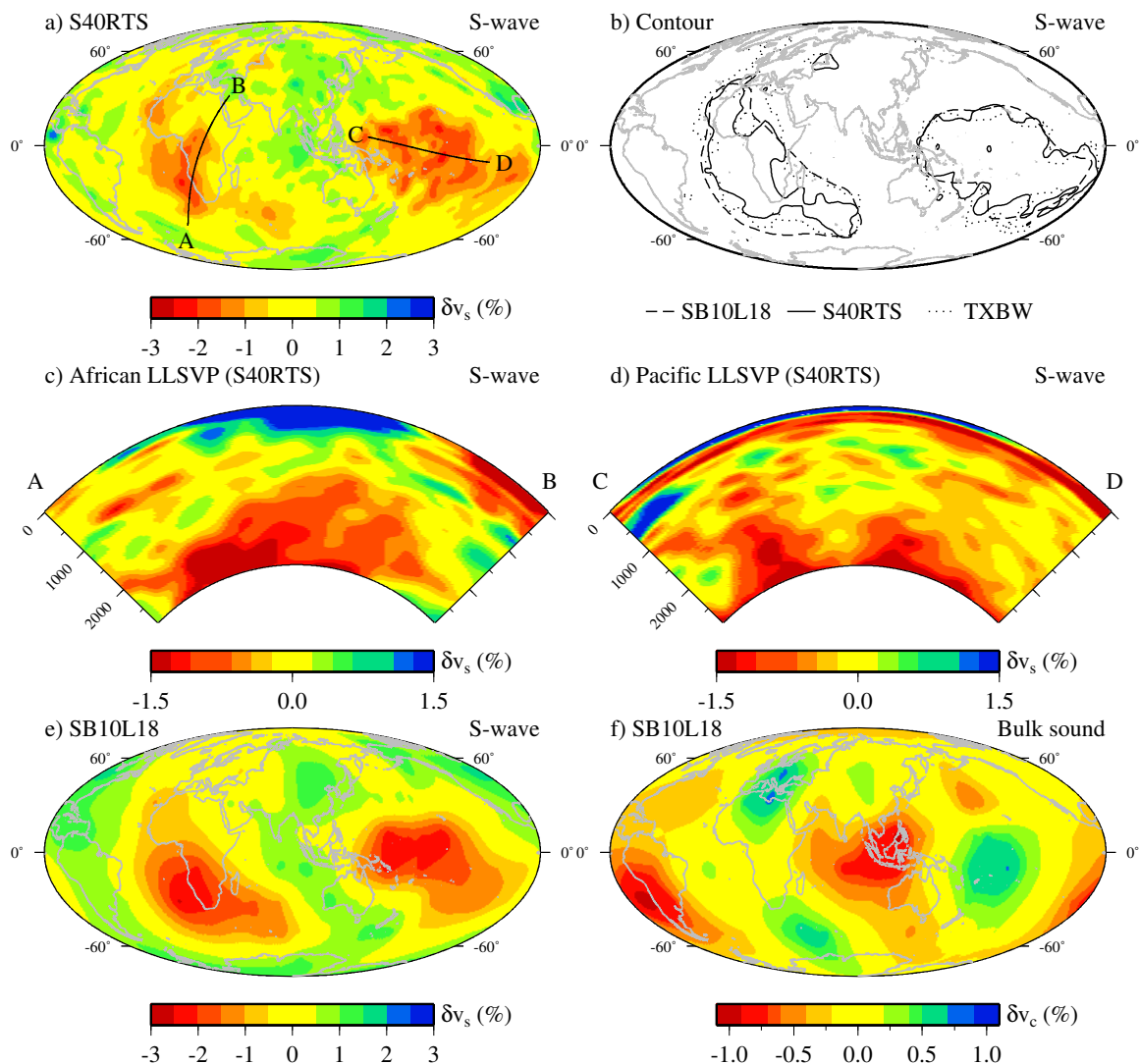


Figure 5.1: Seismic tomography data for the LLSVPs. (a, e) Shear velocity tomography models at 2800 km depth. (a) S40RTS (*Ritsema et al.*, 2011), (e) SB10L18 (*Masters et al.*, 2000). (b) -0.6% shear velocity contours from several S-wave tomography models (SB10L18, S40RTS, TXBW (*Grand*, 2002)) at 2800 km depth show that they are consistent. (c, d) Cross section through the African and Pacific LLSVPs, respectively. The color scale is saturated to highlight mid-mantle structure. Location of cross sections are marked on (a). (f) Bulk sound speed from SB10L18 (*Masters et al.*, 2000) at 2800 km depth. Note approximate anticorrelation with shear velocity in (e).

thickness. However, others favor a moderate basal layer with -3% S wavespeed (e.g., *Ni and Helmberger, 2003b,c*). This later model attributes some of the travel-time delays to the mid-mantle structure, particularly for SKS paths, and thus the basal wavespeed reduction is less. The geographical footprint on the CMB is the same regardless of the vertical extent of the anomaly (e.g., *Wang and Wen, 2004*).

Ni and Helmberger (2003a) model the 3-D geometry of the African LLSVP as a ridge-like structure approximately 1200 km high and 1000 km wide that extends 7000 km along the CMB from Africa to the Indian Ocean. By contrast, the more extreme basal layer model is compatible with a limited and localized mid-mantle extension (e.g., *Wen, 2006*). Definitive confirmation of either model is limited by sparse data coverage for azimuths other than the Drake Passage to Hindu Kush corridor (*Helmberger and Ni, 2005*). 3-D multipathing along strike of the African structure (*Ni et al., 2005; To et al., 2005*) or extreme wavespeed reductions in the basal layer can both explain delayed S-wave postcursors. New seismic tools are being developed to address such ambiguities by helping to distinguish between in-plane (2-D) multipathing caused by horizontal structure and out-of-plane (3-D) multipathing due to vertical structure (*Sun et al., 2009b*).

The African structure also exhibits small-scale features. Ultralow-velocity zones (ULVZs) are detected at the edges of the LLSVP, with one extending at least 800 km along the eastern boundary beneath central Africa (*Helmberger et al., 2000; Ni and Helmberger, 2001a*). Another is located between Madagascar and Africa (*Wen, 2000*) and a third beneath Tristan (*Ni and Helmberger, 2001b*). Shear wave anisotropy

has been interpreted as revealing complex flow occurring at the edges (*Wang and Wen, 2007b*) suggesting strong interactions between the LLSVP and ambient mantle. Recently, *Sun et al. (2010)* provide waveform evidence for a small plume with a diameter less than 150 km emanating from the top of the structure beneath southern Africa.

The Pacific LLSVP is less well imaged than its African counterpart because of source receiver geometry and its location beneath the vast Pacific Ocean. *He and Wen (2009)* construct a comprehensive model along a great arc from East Eurasia to South America using S, Sd, ScS, SKS, and SKKS phase. Their model divides the LLSVP into a western and eastern province separated by a ~ 700 km gap that occurs beneath the Fiji Islands. The western province rises 740 km above the CMB and is 1050 km wide at the base, with edges conjectured to be steeper than the African structure. The eastern section is 340–650 km high and 1800 km wide. This overall geometry is also evident in tomography (e.g., Fig. 5.1d). Each province resembles a trapezoid with a lateral dimension that increases with depth with an S wavespeed reduction of 3% and 5% in the interior and basal portions, respectively (*He and Wen, 2009*). Another cross section from Fiji-Tonga to California uses multibounce S and ScS phases to overcome the lack of stations in the ocean basin (*Liu et al., 2011*). These authors report an overall average height of 600 km with an average anomalous S velocity of -2% and make note of its geometric complexity in comparison to the apparently more simple African LLSVP.

Sharp edges are identified at the margins of the Pacific structure to the south

(*To et al.*, 2005), east (e.g., *Liu et al.*, 2011), and west (*Takeuchi et al.*, 2008). The northeast boundary abuts a ULVZ or a slow basal layer which is overlain by a high-velocity region (~ 120 km thickness) that extends further to the northeast (*He et al.*, 2006; *He and Wen*, 2009). Numerous ULVZs are detected at the southwest margin (see *Thorne and Garnero*, 2004) and a few are situated beneath the LLSVP (e.g., *Liu et al.*, 2011).

Geodynamic calculations have attempted to reproduce the long-wavelength morphology of the LLSVPs; a linear ridge-like feature beneath Africa and a rounded pile beneath the Pacific Ocean. Early 3-D Cartesian thermochemical convection studies with temperature-dependent viscosity only produce ubiquitous ridge-like features (*Tackley*, 1998, 2002). Spherical geometry alone is unable to produce rounded piles without assigning a higher intrinsic viscosity to the LLSVPs, and ridges and piles do not coexist (*McNamara and Zhong*, 2004).

Plate motion history can control the location and morphology of the LLSVPs as shown in models (*McNamara and Zhong*, 2005) that use a global tectonic reconstruction since 119 Ma (*Lithgow-Bertelloni and Richards*, 1998). *Zhang et al.* (2010) recently extended this model by constructing a few, conjectural plate stages back to 450 Ma to further investigate LLSVP mobility and stability using incompressible models with a high-density basal layer. They argue that prior to Pangea formation the African mantle was dominated by downwellings from convergence between Laurussia and Gondwana. The downwellings pushed the chemically distinct material south of Gondwana and into the Pacific hemisphere, forming a single pile. Subsequent

circum-Pangea subduction, particularly on the southeast side of the supercontinent, split the chemical pile into two, forming the African LLSVP. This suggests the Pacific structure has existed since the Early Paleozoic whereas the bulk of the African structure formed at 230 Ma, about 100 Myr after the assembly of Pangea. *Zhong et al.* (2007) show that this implies an interaction of degree-one mantle convection and the supercontinent cycle.

The reconstructed eruption sites of large igneous provinces (LIPs) (since 300 Ma) (*Burke and Torsvik, 2004; Burke et al., 2008*), major hotspots (*Burke et al., 2008*), and kimberlites (since 320 Ma) (*Torsvik et al., 2010*) correlate with the edges of the African and Pacific LLSVPs. *Burke et al.* (2008) therefore propose that the boundaries of the LLSVPs at the CMB are ‘Plume Generation Zones’ (PGZs). This hypothesis suggests that the African and Pacific structures have been independent and stable since before 300 Ma and may be insensitive to plate motions, contrary to the models of *Zhang et al.* (2010). Furthermore, the existence of older LIPs (since 2.5 Ga) suggest LLSVPs earlier in Earth history, although they are not necessarily derived from the same structures that exist today (*Burke et al., 2008*).

A chemically distinct component with a high bulk modulus (high-K) generates structures that satisfy geodynamic and seismic constraints on the LLSVPs (*Tan and Gurnis, 2005, 2007; Sun et al., 2007*). Recent calculations in a spherical geometry reveal the propensity for stronger plumes to develop at the edges of such domes compared to their tops, providing a potential dynamic model for the PGZs (*Tan et al., 2011*). Since high-K structures rely on a balance between thermal and compositional

buoyancy the net density anomaly (relative to ambient mantle) is often small. While this facilitates domes with high relief and sharp, steep boundaries, it may render the structures passive to the circulation induced by plate motions. Subduction zone geometry influences the location of the domes and therefore it may be problematic to maintain the spatial stability of high-K structures for several hundred million years (*Tan et al.*, 2011).

In this study we investigate the stability and morphology of LLSVPs with high-K in a mantle constrained by the tectonic evolution of the lithosphere from 250 Ma to the present. Our models incorporate several advances: (1) a new global tectonic reconstruction (*Seton et al.*, 2012) with continuously closing plate polygons (*Gurnis et al.*, 2012a) that has much finer spatial and temporal resolution while being consistent with the details of global geology; (2) constraints on the thermal evolution of the lithosphere through the assimilation of reconstructed seafloor ages; (3) steering the evolution of slabs in the uppermost mantle using the new tectonic reconstruction and a thermal slab model through progressive data assimilation.

5.3 Numerical models

5.3.1 Governing equations

We apply the extended Boussinesq and Boussinesq approximation (hereafter EX and BO, respectively) (*Ita and King*, 1994) to model thermochemical convection using finite element models. The finite element problem is solved with CitcomS (*Zhong et al.*,

2000, 2008) which is modified to incorporate a depth-dependent chemical density anomaly (e.g., *Tan and Gurnis, 2007*) to simulate the effect of a high bulk modulus material. The equation for the conservation of mass is:

$$\nabla \cdot \mathbf{u} = 0 \quad (5.1)$$

where \mathbf{u} is velocity. The non-dimensional momentum equation is:

$$-\nabla P + \nabla \cdot \underline{\tau} = (\Gamma^{-1} \overline{\Delta\rho_{ch}} C - \bar{\alpha} T) Ra \bar{g} \hat{\mathbf{r}} \quad (5.2)$$

where P is dynamic pressure, $\underline{\tau}$ deviatoric stress tensor, α coefficient of thermal expansion, T temperature, $\Delta\rho_{ch}$ chemical density, C concentration of compositionally distinct material, Ra thermal Rayleigh number, g gravity, and $\hat{\mathbf{r}}$ radial unit vector. Overbars denote radially dependent input parameters and “0” subscripts denote dimensional reference values (Table 5.1). Maximum thermal density anomaly $\Gamma = \rho_0 \alpha_0 \Delta T$, where ρ_0 is density and ΔT is the temperature drop across the mantle.

The Grüneisen parameter (γ) is used *a priori* to construct the depth-dependent chemical density ($\overline{\Delta\rho_{ch}}$) by integrating the self-compression equations for two chemistries with different bulk moduli and zero-pressure density (see *Tan and Gurnis, 2007*, for details). We report the chemical density anomaly at the CMB ($\delta\rho_{ch}$) and the bulk modulus anomaly (δK) (Table 5.2). The usual definition of the buoyancy number, B is recovered for depth-independent chemical density anomaly, $B = \Gamma^{-1} \overline{\Delta\rho_{ch}}$.

Table 5.1: Generic model parameters

Parameter	Symbol	Value	Units	Non-dim Value
Rayleigh number (Eq. 5.3)	Ra	-	-	1.83×10^8
Dissipation number	Di	-	-	1.74
Density	ρ_0	3930	kg m^{-3}	1
Thermal expansion coefficient	α_0	3×10^{-5}	K^{-1}	1
Earth radius	R_0	6371	km	1
Gravity	g_0	10	m s^{-2}	1
Thermal diffusivity	κ_0	10^{-6}	$\text{m}^2 \text{s}^{-1}$	1
Heat capacity	c_{p0}	1100	$\text{J kg}^{-1} \text{K}^{-1}$	1
Temperature drop	ΔT	3000	K	1
Reference viscosity	η_0	5×10^{21}	Pa s	1
Activation energy (Eq 5.7)	E	172	kJ mol^{-1}	6.908
Surface temperature	T_S	300	K	0.1
Heating rate	H	3.2×10^{-8}	W m^{-3}	100
Grüneisen parameter	γ	-	-	2.3

The Rayleigh number is defined as:

$$Ra = \frac{\rho_0 \alpha_0 \Delta T R_0^3 g_0}{\eta_0 \kappa_0} \quad (5.3)$$

where R_0 is Earth radius, η_0 viscosity, and κ_0 thermal diffusivity (Table 5.1). This definition uses the Earth radius rather than mantle thickness and is thus about an order of magnitude larger than the normal definition.

The energy equation (non-dimensional) is:

$$\bar{c}_p \frac{\partial T}{\partial t} = -\bar{c}_p \mathbf{u} \cdot \nabla T + \nabla \cdot (\bar{c}_p \bar{\kappa} \nabla T) - Di(T + T_S) \bar{\alpha} \bar{g} u_r + \frac{Di}{Ra} \mathcal{T} : \dot{\underline{\underline{\epsilon}}} + H \quad (5.4)$$

where c_p is heat capacity, $Di = \alpha_0 g_0 R_0 / c_{p0}$ is dissipation number, T_S is surface temperature, $\dot{\underline{\underline{\epsilon}}}$ is strain rate tensor, and H is internal heating rate (Table 5.1).

The usual definition for the Boussinesq approximation ignores depth-dependent

material properties and heating terms involving Di . However, since high-K structures necessitate pressure-dependent parameters, our BO models only neglect the additional heating terms ($Di = 0$).

The equation for chemical advection is:

$$\frac{\partial C}{\partial t} + (\mathbf{u} \cdot \nabla)C = 0. \quad (5.5)$$

We advect tracers representing the chemical components using a predictor-corrector scheme (*McNamara and Zhong, 2004*) and determine composition using the ratio method (*Tackley and King, 2003*).

5.3.2 Model setup

The full sphere is constructed of 12 caps, each with $128 \times 128 \times 64$ elements, giving a total of ~ 12.6 million elements. Radial mesh refinement provides the highest resolution of 18 km in the boundary layers and a minimum resolution 90 km in the mid-mantle.

High-K domes can form for a range of thermal expansion profiles that decrease with pressure from the surface to the CMB (see *Tan and Gurnis (2007)*, Fig. 3). Conversely, the behaviour of thermal slabs is extremely sensitive to this reduction. Too large of a decrease will invariably hinder and potentially stall downgoing slabs, particularly when coupled with a stiff lower mantle (*Hansen et al., 1991, 1993*). To facilitate interaction between the domes and slabs we therefore opt for a simple parameterization to decrease the thermal expansion coefficient with pressure by a factor

m_α across the mantle:

$$\bar{\alpha} = \frac{1}{2} \left(\frac{r_o - r}{r_o - r_i} + m_\alpha \frac{r - r_i}{r_o - r_i} \right) \quad (5.6)$$

where $r_o = 1$ is the (non-dimensional) outer radius of the sphere and $r_i = 0.55$ is the inner radius. Varying m_α allows us to compare slab descent rates in the lower mantle with estimates using geological tomography correlations (*van der Meer et al.*, 2010). Note that our definition of m_α is different from that used by *Tan and Gurnis* (2007). Our formulation sets the thermal expansion coefficient at the CMB to eliminate a trade-off with the magnitude of the chemical density profile. The thermal expansion at the surface is a factor of m_α larger. Therefore, advective heat transport is enhanced for models with a larger m_α because the effective Rayleigh number is greater, particularly in the uppermost mantle.

Our CMB thermal expansion coefficient is dimensionally $1.5 \times 10^{-5} \text{ K}^{-1}$, which compares favorably with MgSiO_3 perovskite at 88 GPa and 3500 K (*Oganov et al.*, 2001; *Marton and Cohen*, 2002) and is slightly larger than bulk mantle estimates of approximately $1 \times 10^{-5} \text{ K}^{-1}$ (*Stacey*, 1977; *Hama and Suito*, 2001). We define the reference thermal expansion coefficient $\alpha_0 = 3 \times 10^{-5} \text{ K}^{-1}$ (*Stacey*, 1977), which is also comparable with perovskite at ambient conditions (*Katsura et al.*, 2009).

We adopt a purely diffusion creep constitutive relation which is likely to be appropriate for the lower mantle (*Karato and Li*, 1992). Dislocation creep and yielding are critical for the motion of plates and slabs (*Billen and Hirth*, 2007; *Stadler et al.*, 2010). However, because of assimilated plate kinematics and slab structure in the upper mantle (see next section) we effectively remove the need to include these com-

plexities. Viscosity (non-dimensional) is composition dependent:

$$\eta(T, r) = \eta_0(r)(1 + \eta_C C) \exp[E(0.5 - T)] \quad (5.7)$$

where $\eta_0(r)$ is a radially dependent prefactor, η_C is intrinsic compositional viscosity prefactor, and E is non-dimensional activation energy. $\eta_0(r) = 1$ for the lithosphere (0–100 km depth) and $\eta_0(r) = 1/30$ for the upper mantle (100–670 km depth). For the lower mantle $\eta_0(r)$ increases linearly from 2.0 at 670 km depth to 6.8 at the CMB (*Zhang et al.*, 2010). This pressure-induced viscosity increase offsets the decrease caused by the adiabatic temperature gradient. $E = 6.908$ generates 10^3 viscosity variation due to temperature (Table 5.2).

We apply a free slip and isothermal ($T = 1$) boundary condition at the CMB and a kinematic and isothermal ($T = 0$) boundary condition at the top surface. The upper thermal boundary layer is characterized by large velocity gradients and high viscosity due to the temperature-dependent rheology and the imposed $30\times$ step increase from the upper mantle. In the EX framework viscous dissipation produces intense localized heating at plate boundaries. This produces large gradients in strain rate and viscosity which can cause numerical difficulties. Furthermore, a range of deformation mechanisms operate in the lithosphere that cannot be simply modeled by diffusion creep. We therefore set the dissipation number, Di to zero for depths less than 325 km.

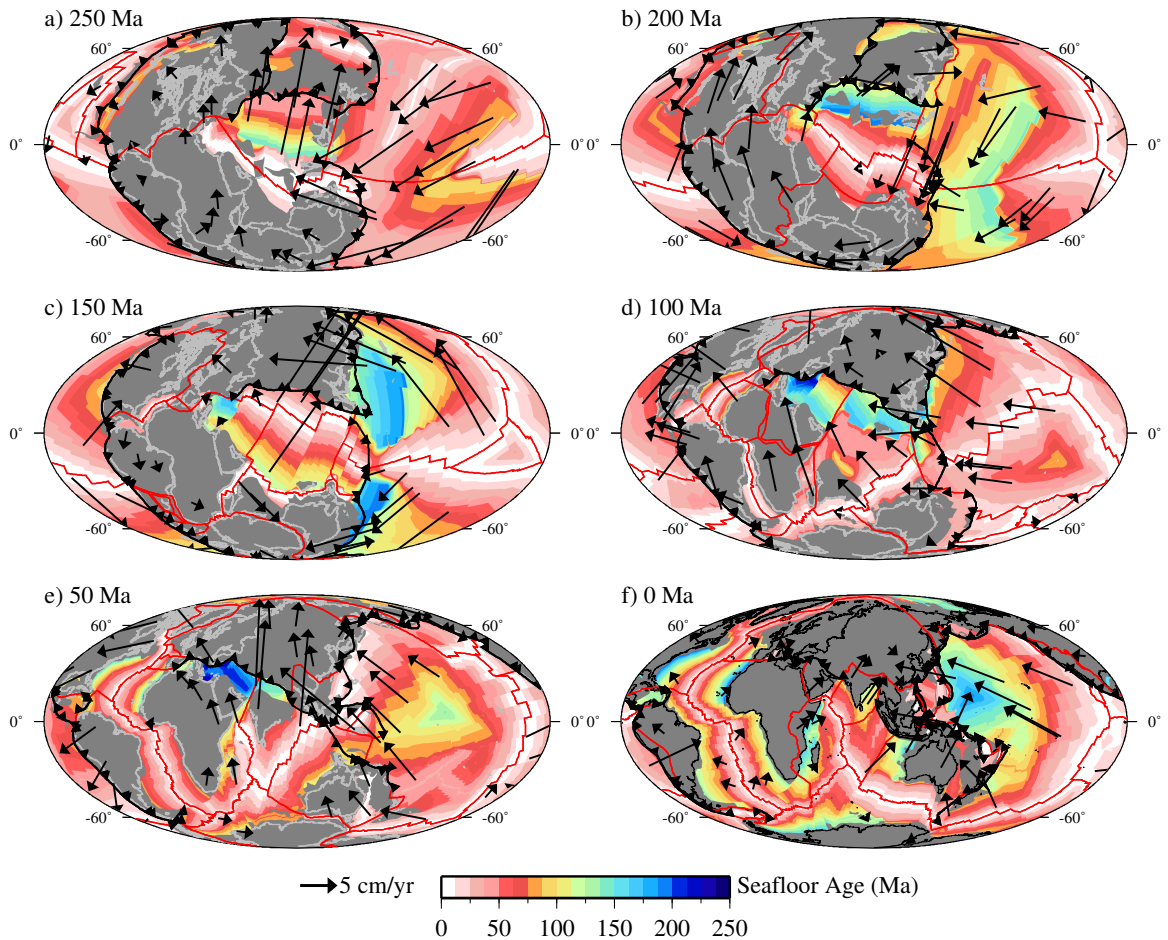


Figure 5.2: Snapshots of the plate tectonic reconstruction (*Seton et al., 2012*) (a) 250 Ma, (b) 200 Ma, (c) 150 Ma, (d) 100 Ma, (e) 50 Ma, (f) present day. Ridges and transform faults are represented by red lines and subduction zones are represented by black lines with sawteeth indicating polarity. Non-oceanic regions are dark grey and reconstructed continents with present-day shorelines are shown in light grey (except black for the present day).

5.3.3 Data assimilation

We use progressive assimilation of a thermal and kinematic model of surface plate evolution with continuously closing plates at 1 Myr intervals (Fig. 5.2) (*Seton et al.*, 2012). The plate motion model is based on a merged moving Indian/Atlantic hotspot reference frame (*O'Neill et al.*, 2005) for the past 100 Myrs and a true polar wander-corrected reference frame (*Steinberger and Torsvik*, 2008) for older times. The Pacific is anchored to fixed Pacific hotspots prior to 83.5 Ma based on a merged *Wessel et al.* (2006) and *Wessel and Kroenke* (2008) reference frame. The proto-Pacific/Panthalassa evolved from an Izanagi-Farallon-Phoenix triple junction. Importantly, the plate model incorporates the break-up of the Ontong Java-Manihiki-Hikurangi plateaus between 120-86 Ma. The Tethys Ocean is reconstructed largely based on a combination of *Stampfli and Borel* (2002) and *Heine et al.* (2004). GPlates (*Gurnis et al.*, 2012a) exports plate velocities from the digitized plate boundary dataset, providing the kinematic boundary condition on the top surface with linear interpolation between the plate model ages. Therefore, in the convection calculations we do not remove net angular momentum or rigid body rotation.

We create a thermal model for the lithosphere using reconstructed seafloor ages and a half-space cooling model (Fig. 5.3). A thermal age of 200 Ma is assigned to non-oceanic regions. At each time step in the computation, for depths ≤ 60 km, the code blends the lithosphere thermal model with the temperature field from the previous time step (see, *Matthews et al.*, 2011, for details). This approach suppresses convective instabilities away from convergent plate margins and dictates the global

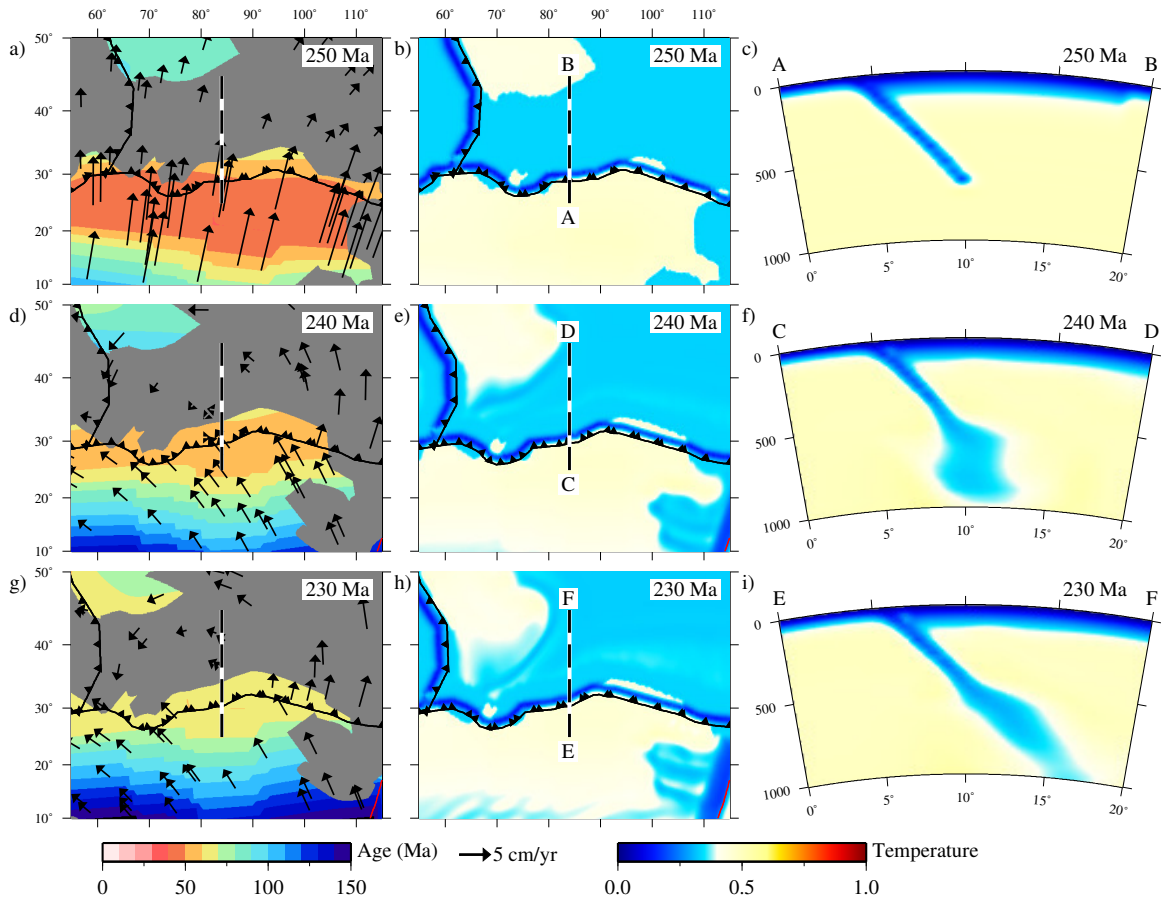


Figure 5.3: Progressive data assimilation example for the convergence of the Paleo-Tethys Ocean and Laurussia (Model EX1). Plate history and age of oceanic lithosphere model (a) 250 Ma, (d) 240 Ma, (g) 230 Ma. Temperature field at 110 km depth (b) 250 Ma, (e) 240 Ma, (h) 230 Ma. Cross section of slab (c) profile A–B, 250 Ma, (f) profile C–D, 240 Ma, (i) profile E–F, 230 Ma. Ridges and transform faults are represented by red lines and subduction zones are represented by black lines with sawteeth indicating polarity. Non-oceanic regions are dark grey.

surface heat flux.

To construct a thermal slab model we use the paleolocation and age of the oceanic lithosphere at convergent plate margins. We then select a slab dip angle (45° for simplicity) and apply a half-space cooling model either side of the slab center line to conserve buoyancy. This thermal structure is assimilated at each time step using a blending stencil. The method ensures that slab buoyancy in the upper mantle is consistent with surface plate evolution and allows our simulations to capture the essential aspects of subduction such as asymmetric geometry and slab roll-back (see, *Gurnis et al.*, 2012b, for details).

5.3.4 Parameter space

The height of high-K domes will adjust according to the height of neutral buoyancy (HNB) as dictated by material properties and temperature contrasts (*Tan and Gurnis*, 2005). To estimate the expected temperature differences we run a preliminary BO model with the same parameters as BO5 (Table 5.2). An internal heating rate $H = 100$ accounts for around 60% of the total heat flux. In the preliminary model, the interior temperature of the domes reaches a steady-state $T \approx 0.83$ (dimensionally ≈ 2800 K) but the ambient material temperature evolves as relatively cold slabs accumulate at the CMB. At 250 Ma (model start time) the ambient material outside of the domes has an average temperature of $T = 0.5$ and cools to $T = 0.43$ at the present day. The assimilation method is not unduly affected by this cooling because the efficient advection of slabs ensures that the uppermost mantle temperature re-

Table 5.2: Model-specific parameters. ^a Lithosphere and slab assimilation. ^b This calculation assumes the domes are 1000 K hotter than ambient material, which is appropriate for the start of the model but evolves as slabs cool the mantle.

Model	Input						Output	
	Approx	Ra	Assim ^a	$\delta\rho_{ch}$ (%)	δK (%)	m_α	η_C	HNB (km) ^b
EX1	EX	1.83×10^8	Y	1.8	6	2	0	700
EX2	EX	1.83×10^8	Y	1.9	9	3	0	700
EX3	EX	1.83×10^8	Y	1.7	4	1	0	700
BO1	BO	1.83×10^8	Y	1.8	6	2	0	700
BO2	BO	1.83×10^8	Y	2.5	6	2	0	-
BO3	BO	1.83×10^8	N	2.5	6	2	0	-
BO4	BO	1.83×10^8	Y	2.5	6	2	100	-
BO5	BO	1.83×10^8	Y	$B = 0.5$		1	0	-
BO6	BO	1.83×10^7	Y	2.5	6	2	0	-

mains close to $T = 0.5$. Rather, the dominant influence of this temperature change is to increase the HNB. Mantle cooling will be less for the EX models because the reduction in the thermal expansion coefficient with pressure will hinder the advection of material and slabs will warm through diffusion. Nethertheless, this basic analysis provides a convenient method to determine the likely evolution of high-K structures without necessitating many expensive computations (Table 5.2).

Tan et al. (2011) generate high-K domes within a spherical geometry free-convection model for density contrasts at the CMB between ≈ 1 –2%. We anticipate requiring upper values from this range for the domes to remain stable during 250 Myrs of tectonic evolution.

5.3.5 Initial condition

Precalculations without data assimilation reveal that about 700 Myr is required for high-K material to develop into high standing structures from an initial layer at the

CMB. At the start of our models (250 Ma) we therefore choose to prescribe two domes centered on the equator at 0 and 180 degrees longitude (for the African and Pacific structures) with a footprint that together occupies 20% of the CMB surface area (Fig. 5.1b). The domes are essentially located in the present day position of the LLSVPs, with the African structure marginally further north and the Pacific structure displaced slightly west (Fig. 5.4a). For simplicity we define a height of 900 km for the domes and accept that this will adjust to the HNB (Fig. 5.4d). The total volume of both structures is approximately $34.4 \times 10^9 \text{ km}^3$ which is comparable to the volume of a 200-km-thick layer residing at the CMB. This volume is about a factor of 2 larger than estimates from seismic tomography (*Burke et al.*, 2008; *Hernlund and Houser*, 2008), but comparable to other geodynamic studies (*McNamara and Zhong*, 2005; *Zhang et al.*, 2010). Additionally, entrainment reduces the size of the structures during the model run.

Ambient mantle is assigned a non-dimensional temperature $T = 0.5$ and in the interior of the structures $T = 0.8$. This approach effectively assumes that most of the domes existed as two coherent and relatively well-mixed structures prior to the early Mesozoic. Thin thermal boundary layers ($\approx 80 \text{ km}$) conduct heat from the CMB and the top of the domes to ambient mantle. The thermal model for the lithosphere and slabs is described in Section 5.3.3. Slabs are initially inserted from the surface to the base of the transition zone (670 km depth).

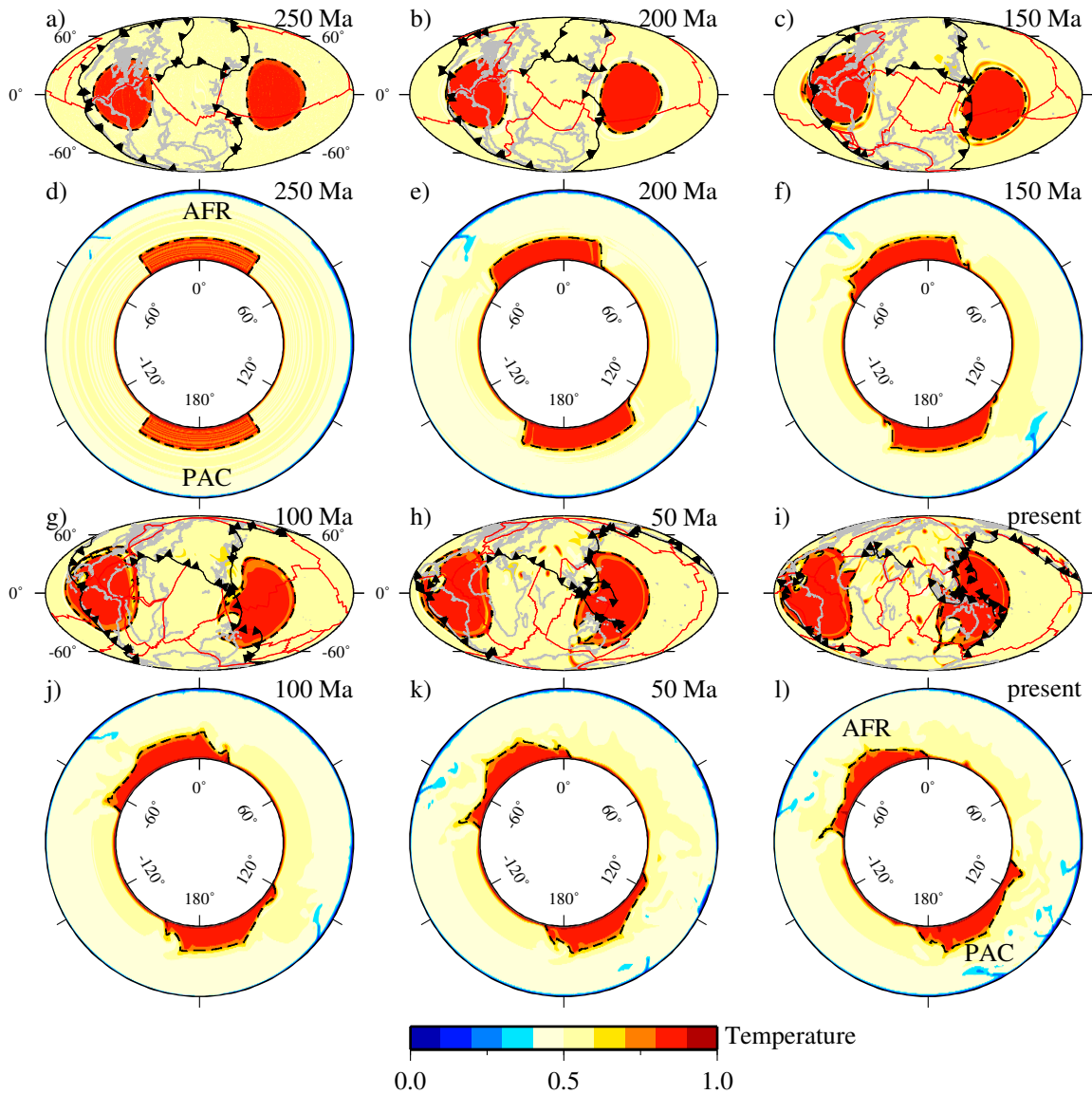


Figure 5.4: EX1 snapshots. (a, b, c, g, h, i) Temperature at 2600 km depth for 250, 200, 150, 100, 50 Ma and present day, respectively. The compositionally distinct material is contoured with black dashed lines. Ridges and transform faults are represented by red lines and subduction zones are represented by black lines with sawteeth indicating polarity. Reconstructed continent outlines are shown in light grey. (d, e, f, j, k, l) Equatorial annuli of temperature (0° is the Prime Meridian) for (a, b, c, g, h, i), respectively. “AFR” and “PAC” identify the domes.

5.4 Results

Fig. 5.4 illustrates the evolution of our reference model (EX1), which also encapsulates the key features of EX2 and EX3 (Table 5.2). During the initial 75 Myrs the African structure is displaced northwards and the Pacific structure southwards (Figs. 5.4a,b,c). The high-K structures retain their steep vertical walls and topography on the interface is negligible. This demonstrates *a posteriori* that the initial thermal and compositional structure for the domes (Fig. 5.4a,d) is dynamically compatible with the parameters of the calculations. Plate motions then shift both structures westward from ~ 175 Ma to present day (Fig. 5.4g,h,i). The final position of the African structure is beneath the Atlantic Ocean and South America, while the Pacific structure is beneath the western Pacific Ocean and Australasia (Fig. 5.4i).

Neither dome experiences significant deformation since the initial prescribed geometry is largely retained. However, subducting slabs generate stresses that deflect the top interface of the domes and can produce extensive topography. For example, slabs originating from Central American subduction depress a western portion of the African structure by several hundred kilometers (Fig. 5.4k,l, at -60°). Circular embayments punctuate the edge of the domes (Fig. 5.5, green arrows). These produce tendrils of chemically distinct material that extend away from the structures and join ridges of thickened boundary layer of ambient material (Fig. 5.5, red arrow). Slabs are generally contained within the upper half of the mantle and do not accumulate at the CMB.

Classical thermal plumes (spheroidal plume head followed by a tail) of ambient

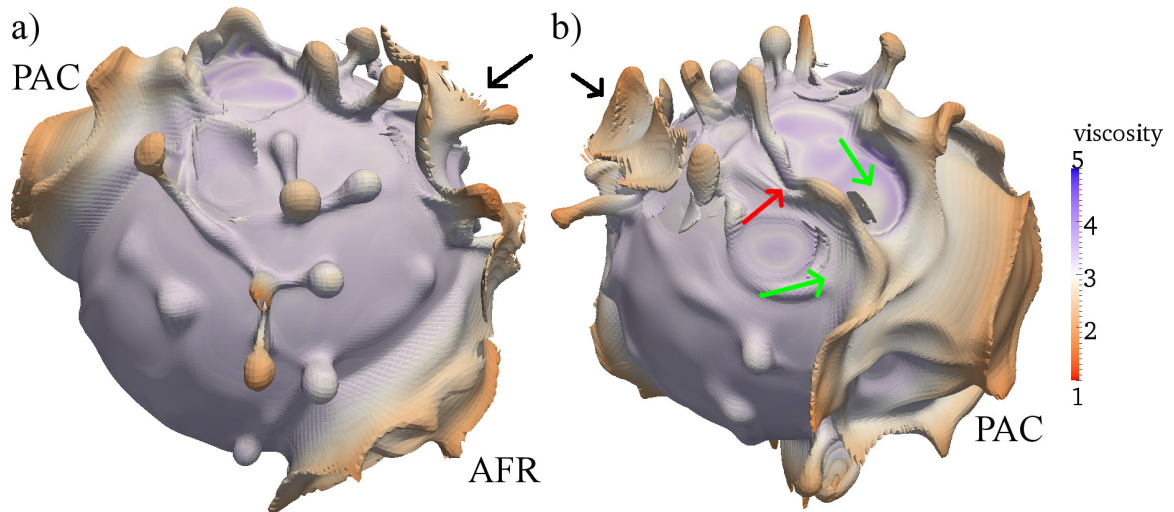


Figure 5.5: Thermal plumes rising from ridges between the domes at present day (EX1). The $T = 0.6$ isosurface is coded by viscosity for depth perception (viscosity is pressure dependent). (a) View from the North Pole. The Pacific (PAC) and African (AFR) structures are the prominent red-capped mesas. The contiguous band of elevated temperature that is disconnected from the CMB is caused by dissipative heating from Tethyan slabs (black arrows). (b) View centered on $(90^\circ, 0^\circ)$ showing the western edge of the Pacific dome, circular embayments (green arrows), and tendrils extending from the domes (red arrow)

material develop from interconnected ridges of thickened boundary layer at the CMB. These are generally located away from the domes (Fig. 5.5) with more upwellings beneath Africa and Eurasia than the Pacific region. The high-K structures develop a perimeter of thickened boundary layer, although the edges are not preferred regions of plume formation.

EX2 and EX3 have different drops in thermal expansion across the mantle (factor of 3 and 1, respectively) and chemical density profiles compared to EX1. With a comparable HNB these models are qualitatively similar to the reference model. The domes in EX2 are marginally flatter with less edge deformation, and plume activity is also reduced. Conversely, the structures in EX3 stand a little higher from the CMB and have steeper sides. In this model, downwellings more significantly deform the domes. For example, Central American slabs produce sufficient stresses to generate a large circular embayment in the north of the African structure. To a lesser extent, displacement of material away from Central America also occurs in EX1 (Fig. 5.4g,h,i).

The Boussinesq equivalent of EX1 (BO1) does not produce stable domes (Fig. 5.6). Slabs are stronger in BO1 because they have more thermal buoyancy, and are therefore cooler and more viscous at all mantle depths because the transit time through the mantle is reduced (~ 50 Myr). The slabs exert large stresses on the side walls of the domes and can slide beneath the high-K structures, further destabilizing them. Ultimately the domes rise off the CMB (Fig. 5.6f). In BO2, we increase the density contrast at the CMB ($\delta\rho_{ch}$) whilst retaining the same bulk modulus anomaly. In this model, the structures remain stable at the CMB until ~ 70 Ma (Fig. 5.7c,e).

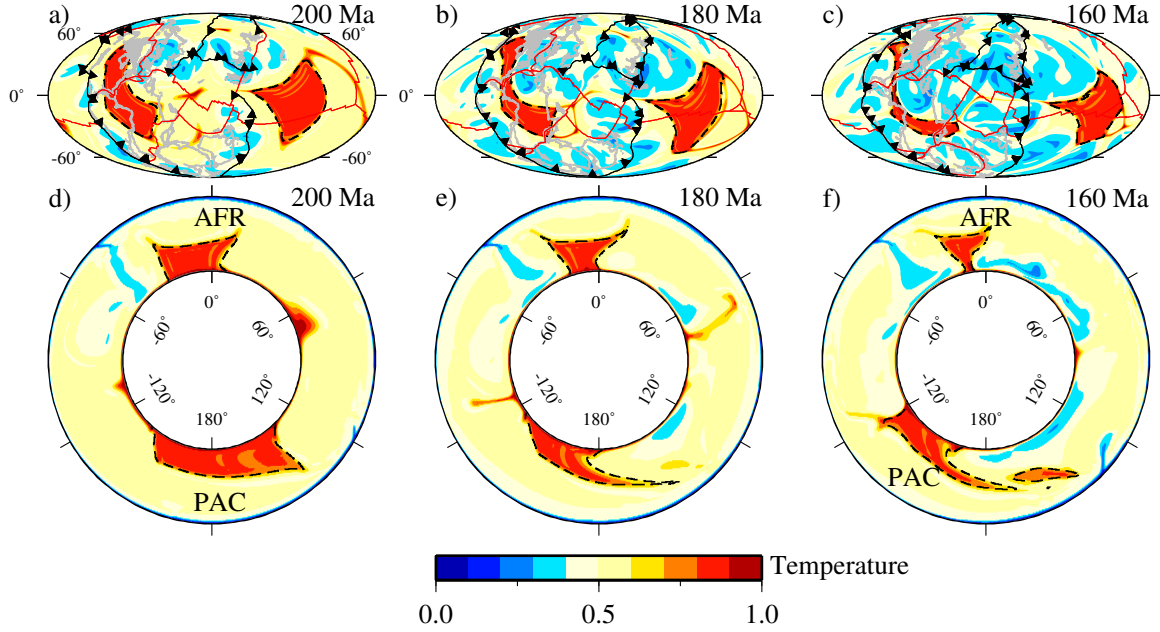


Figure 5.6: BO1 snapshots. (a, b, c) Temperature at 2600 km depth for 200, 180, 160 Ma, respectively. (d, e, f) Equatorial annuli of temperature (0° is the Prime Meridian) for (a, b, c), respectively. For details, see Fig. 5.4 caption.

Additionally, entrainment reduces the size of the domes, particularly the African anomaly.

BO5 does not include a high-K component, but the evolution of the model from 250 to 70 Ma is similar to BO2 (compare Figs. 5.8h,k and Figs. 5.7c,e). In comparison to BO2, BO5 achieves both stable domes and less entrainment (Fig. 5.8), although the domes do not stand as high above the CMB and their edges are less steep. This is particularly evident for the African anomaly. Nevertheless, in these cases the lateral migration of the domes at the CMB is insensitive to the details of the chemically distinct high-K or uniform density material. We therefore expect that BO5 is representative of high-K models with stable domes and minimal entrainment, excluding the vertical extent of the structures.

The domes initially flatten in BO5 because they are more dense than in the previ-

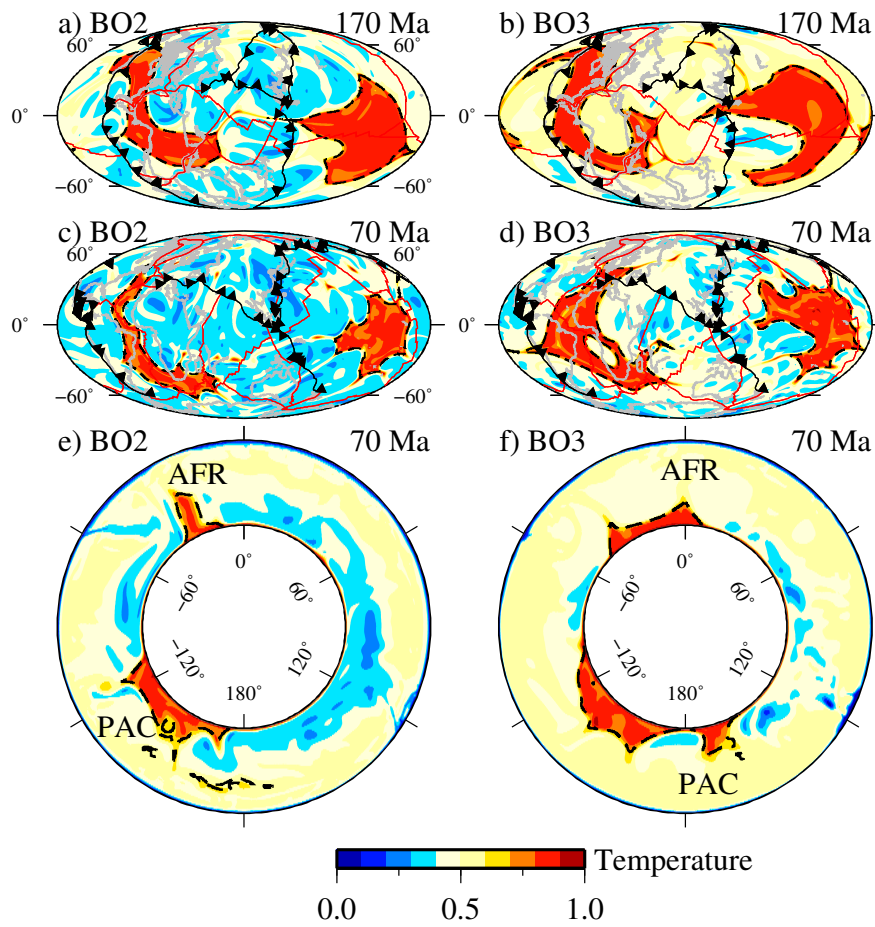


Figure 5.7: BO2 (with assimilation) and BO3 (kinematic only) snapshots. Temperature at 2600 km depth for (a, c) BO2 at 170 and 70 Ma, respectively. (b, d) BO3 at 170 and 70, respectively. (e, f) Equatorial annuli of temperature (0° is the Prime Meridian) for (c, d), respectively. For details, see Fig. 5.4 caption.

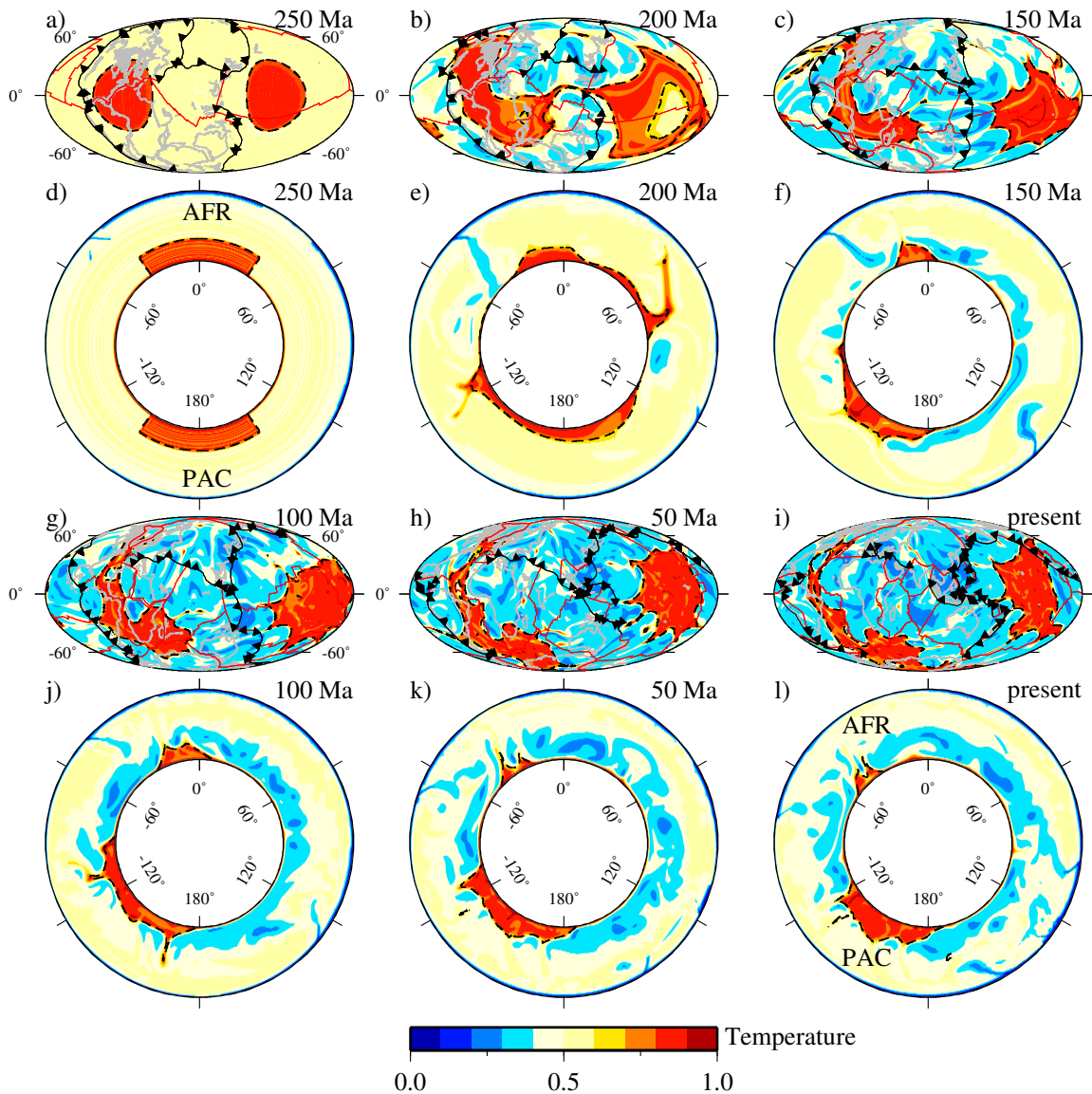


Figure 5.8: BO5 snapshots. (a, b, c, g, h, i) Temperature at 2600 km depth for 250, 200, 150, 100, 50 Ma and present day, respectively. The compositionally distinct material is contoured with black dashes. Ridges and transform faults are represented by red lines and subduction zones are represented by black lines with sawteeth indicating polarity. Reconstructed continent outlines are shown in light grey. (d, e, f, j, k, l) Equatorial annuli of temperature (0° is the Prime Meridian) for (a, b, c, g, h, i), respectively. For details, see Fig. 5.4 caption.

ous high-K models, which increases their CMB footprint throughout the model run. Descending slabs promote thickening of the lower thermal boundary layer and a few short-lived plumes develop at the edges of the domes. The domes deform readily in response to slabs but have sufficient intrinsic density contrast to remain stable at the CMB. They can develop steep edges from boundary tractions caused by slab-induced flow (for example, the eastern edge of the Pacific anomaly, Fig. 5.8l, at -120°). Elsewhere the edges are tapered, such as the western boundary of the Pacific structure (Fig. 5.8l, at 180°).

In BO5, from 250 to 200 Ma, the African and Pacific structures are displaced northwards and southwards, respectively, similar to EX1. Around 200 Ma the Pacific dome is indented by western Pacific slabs that produce two embayments along its boundary (Fig. 5.8b). Slabs from North and South America inhibit the African structure from advancing west while slabs from Africa-Eurasian collision displace material from North Africa (Fig. 5.8c). This elongates the African dome north-south in the northern hemisphere and west-east in the southern hemisphere. The African structure migrates slightly westward as seafloor spreading in the South Atlantic Ocean moves Africa northeastward (Fig. 5.8h). During this time slabs continue to pile up beneath present day Africa (Fig. 5.8i). The Pacific structure is slightly elongated north-south by circum-Pacific slabs from 100 Ma and is centrally located beneath the Pacific Ocean at present (Fig. 5.8i).

Central American slabs slice a small region from the African structure around 230 Ma (small structure to the southwest of the main African anomaly in Fig. 5.8b). This

material migrates southwestward and eventually merges with the Pacific structure at ~ 200 Ma. Additionally, the African dome develops a limb at 200 Ma that extends beneath northwest North America (Fig. 5.8c). This extension merges with the northwest boundary of the Pacific dome around 140 Ma, and slabs eventually detach the limb from the main African structure at 100 Ma.

Geodynamic studies often apply a purely kinematic boundary condition to the top surface of models to produce downwellings at convergent plate margins. However, with this approach it is not clear if the downgoing buoyancy flux is reasonable for the convergence rate and lithospheric buoyancy predicted by geologically consistent plate reconstructions. Therefore, we compare the influence of lithosphere and slab assimilation (BO2) with a purely kinematic boundary on the top surface (BO3) (Fig. 5.7); all model parameters are otherwise identical. The assimilation method increases slab flux into the lower mantle and the domes have steeper sides and reduced volume.

McNamara and Zhong (2004) demonstrate that an intrinsic viscosity increase in the chemically distinct material can control the style of deformation of the domes. In comparison to BO2, the domes in BO4 have a factor 100 intrinsic viscosity increase. The first downwellings to reach the CMB perturb the lower thermal boundary and generate plumes both at the edges of the domes and away from the structures. From 250 Ma to present, the domes remain as individual coherent structures and do not exchange mass between each other. The topography on the top of the domes is largely unperturbed. At present, the domes are located similarly to BO5 (Fig. 5.8i), except

the African structure is more localized beneath the South Atlantic Ocean and South America and the Pacific structure is rounder.

A reduced Rayleigh number ($Ra = 1.83 \times 10^7$) decreases the sinking rate of slabs because it is equivalent to increasing the background viscosity uniformly (BO6). Convection is more sluggish and its characteristic length-scale larger. From 250 to 150 Ma, the evolution of BO6 is akin to EX1 (Fig. 5.8i) where the domes migrate north and south for the African and Pacific structures, respectively. Around 110 Ma, Central American slabs carve a portion of the African structure which merges with the Pacific dome at ~ 80 Ma. This is similar to the behavior in BO5 although the timescale is increased for the lower Ra model. At present, the African structure is elongated north-south and located beneath the Atlantic Ocean with its eastern margin roughly following the African coastline. The Pacific structure is stretched west-east and located beneath the Pacific Ocean, although preferentially to the west.

5.5 Discussion

The models broadly fall into two classes, depending on whether the domes are predominantly affected by the buoyancy of subducting slabs or by coupling to surface plate motions. The EX models are dominated by coupling to plates and slab buoyancy is weak (“weak-slab models”). In contrast, the BO models are most influenced by downwellings that accumulate at the CMB (“strong-slab models”).

At present day the high-K structures are marginally flatter in EX2 and steeper-sided in EX3, relative to EX1. Nevertheless, for the weak-slab models, each dome

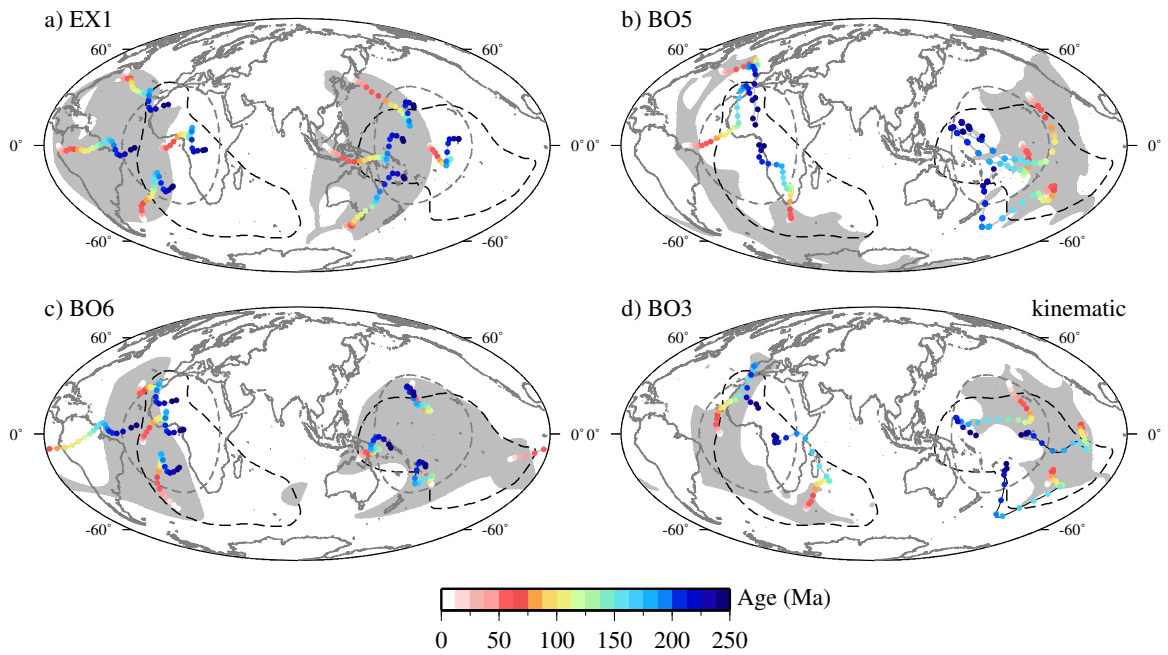


Figure 5.9: Motion and deformation of the domes at 2600 km depth, (a) EX1, (b) BO5, (c) BO6, (d) BO3. The grey-shaded region shows the domes at present day and the dark grey dashes contour the initial position of the domes at 250 Ma. Black dashes delineate the -0.6% S-wave contour from SB10L18 and continent outlines are shown in solid dark grey. Color-coded dots show the movement of the domes from 250 Ma to present day.

follows a similar course as it migrates along the CMB and its present day location is comparable (Fig. 5.9a). From 250 to 150 Ma, the African and Pacific structures move to the north and south, respectively. Dominant motion is then westward from 150 Ma to present day. Both domes are displaced between 35° (Pacific) and 45° (African) west of their initial position at 250 Ma. The Pacific dome lies beneath many of the western Pacific subduction zones, which seems contrary to the hypothesis that chemical layers are displaced away from downwellings (*Davies and Gurnis, 1986; McNamara and Zhong, 2005*). However, domes may exist beneath subduction zones if they have only recently initiated. For example, Tonga overlies the edge of the Pacific LLSVP, but is relatively young, having only formed since 45 Ma (*Gurnis et al., 2000*). A weak slab push force does not overly influence the morphology and location of the structures. Therefore the high-K structures are stable and generally coherent with sharp steep walls, similar to models without slabs (*Tan and Gurnis, 2005, 2007*). However, downwellings can generate significant topography on the domes and locally displace material from some regions of the CMB.

Slabs in the strong-slab models with lithosphere and slab assimilation can propagate to the CMB and deform and displace the domes. From 250 to 200 Ma, the Paleo-Tethys seafloor is relatively old and introduces a large amount of negative buoyancy into the mantle at the trench through slab assimilation. This is compounded by the Tethyan/Mongol-Okhotsk triple junction (trench-trench-trench) (Fig. 5.2), and slabs pile up on the CMB and push material southwestward toward (and ultimately beyond) present day Africa (Fig. 5.9b). This deforms the African structure into an

elongated kidney shape that migrates southwestward after the opening of the South Atlantic Ocean. By contrast, the seafloor is generally younger at the North and South America trenches and the assimilated slabs have less negative buoyancy and a smaller viscosity contrast. Therefore these slabs are weaker and unable to counter the motion of the African dome to the southwest caused by Tethyan slabs. Nevertheless, the ridge-like morphology of the African structure agrees with tomography (Fig. 5.1), waveform modeling (*Ni and Helmberger, 2003b*), and other geodynamic studies (e.g., *McNamara and Zhong, 2005*).

The Pacific structure migrates eastward in the strong slab models, which contrasts with predominant westward motion in the weak-slab models (Fig. 5.9a,b). This is because slabs from the western Pacific subduction zones are dominant in pushing the dome beneath the Pacific Ocean. Tomographic inversions suggest that the basic morphology of this structure is a rounded pile slightly elongated in longitude (Fig. 5.1). Our Pacific dome is generally well located, although slightly extended in the latitudinal direction. This implies that slabs originating from subduction zones in the north and south Pacific (versus the west and east margins) are less dominant in shaping the boundaries of the dome.

A purely kinematic surface boundary condition (BO3) displaces and deforms the domes similarly to models with lithosphere and slab assimilation (Figs. 5.9b,d). In BO3, the African and Pacific structures align more closely with tomography and the Pacific structure is elongated west-east. However, the vertical extent of the structures varies significantly despite the same high-K parameters (Fig. 5.7). The

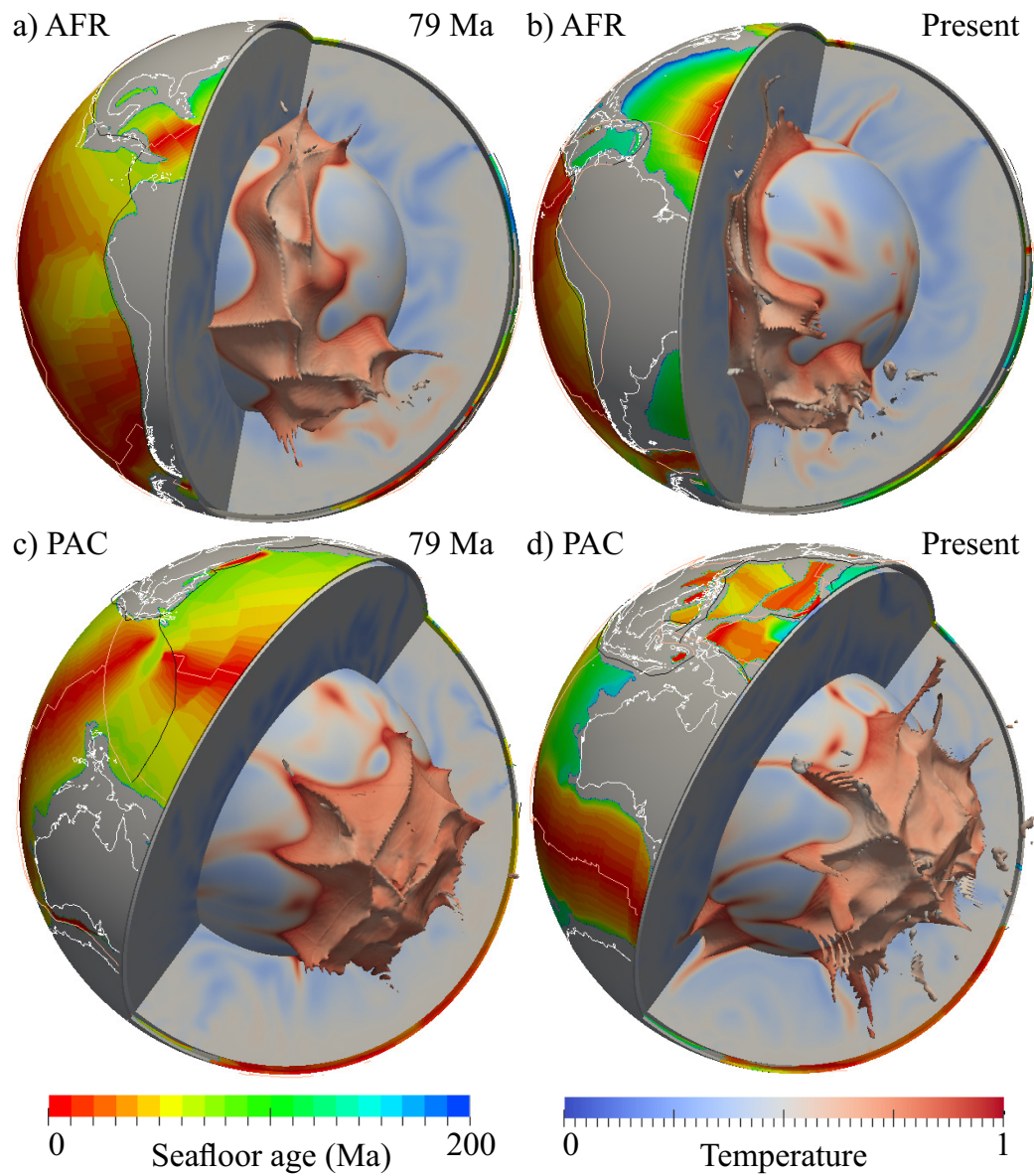


Figure 5.10: 3-D view of the domes in model BO5. African structure at (a) 79 Ma, (b) Present. Pacific structure at (c) 79 Ma, (d) Present. Ridges and transform faults are represented by red lines and subduction zones are represented by black lines. Non-oceanic regions are dark grey and reconstructed continents with present day shorelines are shown in white.

assimilation method increases the down flux into the lower mantle, which has two main effects. First, the stronger slab push steepens the boundaries of the domes. Second, the lower mantle is more efficiently cooled, which raises the HNB of the high-K structures. Therefore, with realistic slab fluxes we expect high-K structures to be less stable than the prediction from models with purely kinematic boundary conditions.

Domes with increased intrinsic viscosity (BO4) do not deform readily in response to slabs, retain a relatively flat top, and become hotter because convection is inhibited (*McNamara and Zhong, 2004*). However, the lateral motion of the structures is not unduly affected because of the free-slip boundary condition at the CMB.

For BO6 ($Ra = 1.83 \times 10^7$), the shape and areal extent of the domes at 2600 km depth correlate fairly well to tomography (Fig. 5.9c). The African structure is displaced too far west although the mismatch is less than for the other models. A sliver of the African dome is carved from the main anomaly by slabs from Central American subduction, which eventually merges with the eastern boundary of the Pacific structure (Fig. 5.9c, leftmost tracer). This demonstrates how mass transfer between the domes (*McNamara et al., 2010*) may be intimately linked to paleogeography.

The “weak-slab models” arise from the extended-Boussinesq approximation. Adiabatic and viscous heating are often ignored in convection calculations because they are in balance globally (e.g., *Leng and Zhong, 2008*). However, even though some previous studies neglect these terms (*McNamara and Zhong, 2005; Zhang et al., 2010; Steinberger and Torsvik, 2011*) they contribute significantly to dissipate the ther-

mal anomaly of slabs in our EX models. It is uncertain how these dissipative terms interact with model parameters and data assimilation.

Steinberger and Torsvik (2011) (hereafter ST11) recently developed a geodynamic model to investigate plume formation at the edges of the domes by prescribing a slab buoyancy flux constrained by global plate reconstructions. BO6 has a comparable Rayleigh number to ST11, yet the location of their domes at the CMB agrees better with seismic tomography. We attribute the difference to two major factors.

First, ST11 apply the plate model to determine the depth-integrated density anomaly of oceanic lithosphere at the trench. This truncates the maximum slab buoyancy to the equivalent of 80 Ma seafloor, whereas our half-space model includes more buoyancy for older slabs. ST11 further reduce slab buoyancy by 21% to account for the subduction of crust and depleted mantle. This means their slab buoyancy is significantly reduced for all subduction zones, and particularly those with subducting plates older than 80 Ma (notably the Tethyan region at certain ages). The plate model therefore likely mitigates the Tethyan slab push that migrates the African dome in our models to the southwest.

Second, the location of paleosubduction influences the evolution of the domes. The subduction models used in ST11 (*Steinberger and Torsvik*, 2010) and this study (*Seton et al.*, 2012) appear qualitatively similar, but it remains unknown how the evolution of specific regions affects the deep-Earth structure. ST11 also apply a longitudinal shift to subduction zone locations (*van der Meer et al.*, 2010) which improves their dome fit to tomography. Applying a similar rotation to our plate

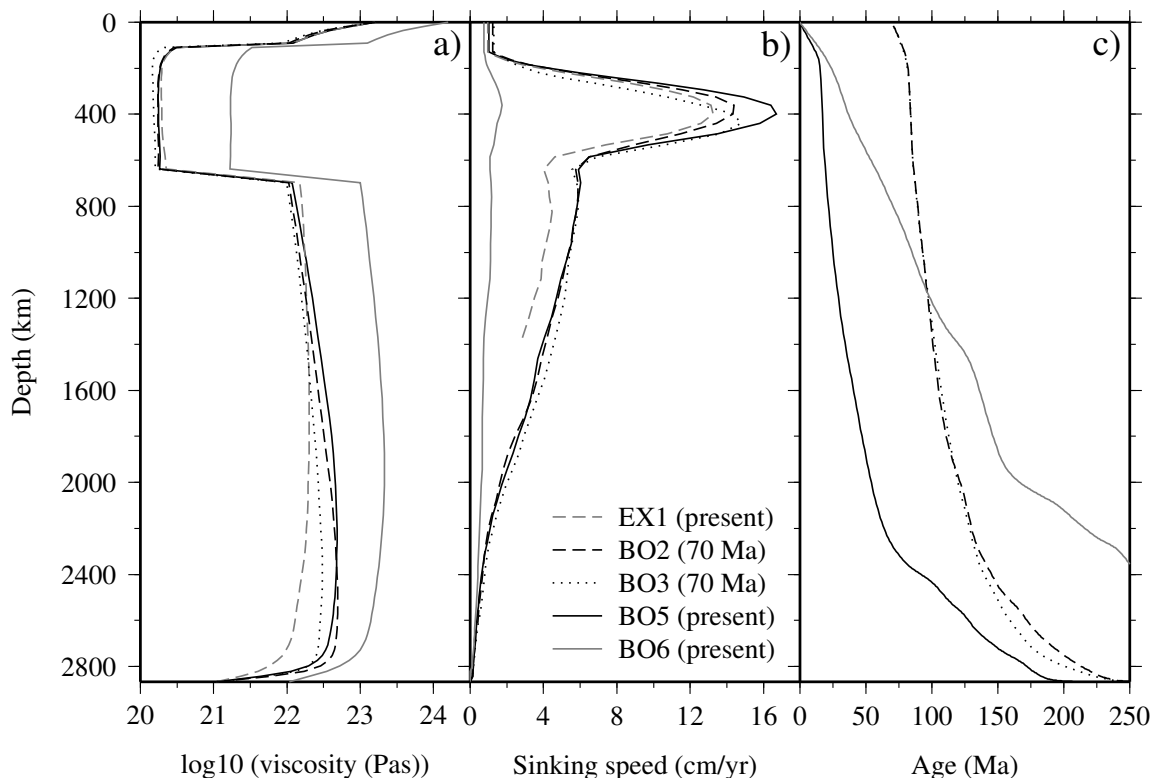


Figure 5.11: Radial profiles for (a) Viscosity, (b) Slab sinking speed, (c) Approximate age of subducted material versus depth, for EX1, BO5, BO6 at present day, and BO5, BO6 at 70 Ma. Sinking speed is determined from positive density anomalies that are greater than 25% of the maximum positive density anomaly at each depth and time (e.g., *Steinberger and Torsvik, 2010*). We set the velocities for depths < 128 km to the value at 128 km depth because they are influenced by data assimilation. The age-depth relation is computed by integrating the time- and depth-dependent slab sinking speed.

history model may enforce the migration of the African dome to the southwest and increase the mismatch.

The slab sinking rate for most of the models here is larger than geological estimates (e.g., 1.2 cm yr^{-1} , *van der Meer et al., 2010*), except for BO6 (Fig. 5.11c). BO6 has a lower Rayleigh number, which is equivalent to a ubiquitous increase in mantle viscosity (Fig. 5.11a). The Stokes sinking velocity is proportional to the driving density contrast and inversely proportional to the background viscosity. Slabs in EX1

do not retain a strong thermal anomaly for depths > 1400 km because the temperature anomaly is dissipated (Fig. 5.11b). BO2 (with assimilation) and BO3 (purely kinematic) at 70 Ma have approximately the same age-depth relation (Fig. 5.11c), despite the significantly increased lower-mantle slab flux from slab assimilation. This is because cooler material in the lower mantle reduces the driving density contrast for subsequent downwellings. Furthermore, the bulk background viscosity increases through the temperature-dependent rheology, which further reduces the sinking velocity of slabs (Fig. 5.11a). BO3 actually has a marginally faster sinking rate throughout the lower mantle.

We observe plumes forming at the edges of the domes (*Tan et al., 2011; Steinberger and Torsvik, 2011*) from thickened boundary layer pushed toward the structures by slabs. However, plume formation is partly controlled by the maturity (thermal buoyancy available at the CMB) and stability of the lower thermal boundary. Since the most prominent edge-activity occurs during the early stage of the model we relate this largely to the initial condition and the lack of preexisting plume conduits. Furthermore, a 250 Myr integration time is not sufficient for a statistical analysis of plume distribution.

For the high-K structures in the strong-slab models (BO2, BO3, BO4, BO6), the chemical density anomaly is larger than the thermal density anomaly across the whole mantle pressure range. Therefore a HNB does not exist and the high-K material effectively replicates a high-density layer. We consider the density anomaly at the CMB (relative to ambient material) for high-K material, $\Delta\rho_k$, and slab, $\Delta\rho_s$. High-K struc-

tures form when $\Delta\rho_k < 0$, and to ensure they remain stable in the presence of slabs requires $\Delta\rho_k > \Delta\rho_s$. However the latter relation cannot be true because $\Delta\rho_s > 0$. Therefore, slabs will always have a tendency to sweep beneath high-K structures unless $\Delta\rho_k$ is large and thermal buoyancy no longer dominates at depth. Furthermore, the hot domes have low viscosity and therefore deform readily in response to stresses from stiffer slabs. This further enables slabs to compromise stability by sliding beneath the domes. Higher intrinsic viscosity for the high-K structures can mitigate this effect (BO4).

5.6 Conclusions

We present models that investigate the stability and morphology of high bulk modulus structures in the lower mantle from 250 Ma to present day with constraints from paleogeography. The domes in “weak-slab” models are strongly coupled to plate motions and migrate along the CMB as coherent structures without significant deformation. These structures are displaced 35 to 45 degrees west of their inferred position from seismic tomography. In contrast, the domes in ‘strong slab’ models deform and migrate along the CMB in response to slab stresses. These models produce a ridge-like anomaly beneath Africa and a rounded pile beneath the Pacific Ocean, similar to previous studies. However, the African structure is displaced too far southwest in comparison to seismic modeling. This is because the progressive assimilation method produces strong Tethyan slabs that deform the African dome into a kidney shape and displace the structure to the southwest beyond present-day Africa.

High-K structures rely on a delicate dynamic balance between thermal and chemical buoyancy; they are almost neutrally buoyant because net density differences are small. Therefore, high-K domes are passive components and the flow is largely imposed by plate motions and slabs. Even “weak slabs” produce notable topography on the surface of the high-K structures and can locally displace material from some downwelling regions (e.g., Central America). “Strong slabs” that are more dense and more viscous than the structures generate stresses that can compromise the stability of the domes at the CMB. Additionally, these slabs can further steepen the edges of high-K structures (or uniform dense layers) and may slide beneath the domes, which can cause the structures to raise off the CMB. Relative to models without slabs, the parameter space for stable high-K structures appears to be reduced.

Finally, our study also outlines a new modeling framework to utilize paleogeography constraints from plate history models to chart the evolution of deep mantle structures. This modeling suggests that the assimilation method increases the slab buoyancy flux relative to models with a purely kinematic boundary condition on the top surface.